Research Square

Preprints are preliminary reports that have not undergone peer review.
They should not be considered conclusive, used to inform clinical practice,
or referenced by the media as validated information.

Turnip crinkle virus coat protein determines whether salicylic acid promotes or restricts infection

Dana Rademacher
University of Missouri - Kansas City
Braeden Kingsolver
University of Missouri - Kansas City
Akashata Dawane
University of Missouri - Kansas City
Jared May
jpmay@umkc.edu

University of Missouri - Kansas City https://orcid.org/0000-0002-0671-5643

Research Article

Keywords: Turnip crinkle virus, salicylic acid, plant virus, coat protein, viral pathogenesis, hypersensitive response, plant antiviral immunity, transcriptomics, Arabidopsis thaliana

Posted Date: November 4th, 2026

DOI: https://doi.org/10.21203/rs.3.rs-8695072/v2

License: This work is licensed under a Creative Commons Attribution 4.0 International License.
Read Full License

Additional Declarations: The authors declare no competing interests.

Turnip crinkle virus coat protein determines whether salicylic acid promotes or restricts infection

Dana J. Rademacher[1], Braeden Kingsolver[1], Akashata Dawane[1], and Jared P. May[1*]

[1]Division of Biological and Biomedical Systems, University of Missouri – Kansas City, Kansas City, Missouri, USA

*Address correspondence to: Jared P. May, jpmay@umkc.edu

Summary

Turnip crinkle virus (TCV) coat protein (CP) coordinates virion assembly, immune recognition, and RNA silencing suppression, but how these functions shape disease remains unclear. We redirected CP from the nucleus by appending an identical nuclear export signal to either terminus. Despite similarly reducing nuclear CP accumulation, N- and C-terminal modifications produced opposing effects on disease, viral accumulation, particle formation, and HRT-mediated recognition, indicating that sustained nuclear CP is dispensable for these outcomes. Transcriptomic and biochemical analyses revealed that disease severity closely tracked salicylic acid (SA) accumulation. Genetic disruption of SA biosynthesis reduced chlorosis and necrosis, establishing SA as a driver of TCV-associated disease. However, SA had CP-dependent effects on viral accumulation, promoting WT and N-NES infection while restricting C-NES. The R6A CP mutant uncoupled disease from viral burden, inducing SA and severe symptoms despite reduced accumulation. Thus, CP determines SA induction and whether an SA-rich environment favors or restricts TCV.

Introduction

Plant virus coat proteins are increasingly recognized as multifunctional regulators of infection rather than simple structural components of the virion.[1] In addition to encapsidating the viral genome, coat proteins can regulate cell-to-cell and systemic movement, suppress antiviral RNA silencing, interact with host defense proteins, and alter cellular signaling.[2-6] These functions often require coat proteins to occupy multiple subcellular compartments, including cytoplasmic compartments and the nucleus.[7] However, experimentally manipulating coat protein localization can be difficult to interpret because the same regions that mediate intracellular targeting may also participate in RNA binding, particle assembly, or interactions with host factors.[8-10]

Turnip crinkle virus (TCV) provides a well-defined system for investigating these overlapping coat protein functions. TCV contains a single-stranded positive-sense RNA genome encapsidated within a T=3 icosahedral particle composed of 180 copies of the viral coat protein (CP).[11] Structurally, TCV CP contains an N-terminal RNA-interacting region positioned within the virion and C-terminal domains that form the particle shell and surface-exposed projections.[12] CP is also required for efficient systemic infection and functions as a potent viral suppressor of RNA silencing.[13,14] Additionally, CP is an important determinant of immunity in *Arabidopsis thaliana*. In resistant *Arabidopsis* accessions carrying the HRT resistance protein,[15] the N-terminal region of CP serves as an avirulence determinant and contributes to activation of the hypersensitive response (HR).[16] This region also contains determinants implicated in interaction with the NAC transcription factor TCV-interacting protein (TIP/ANAC091) and in CP nuclear localization.[17] Previous studies reported the formation of CP-containing nuclear foci and

found that exclusion of CP from the nucleus impaired HRT-mediated necrosis in *Nicotiana benthamiana*, suggesting an important role for nuclear CP during incompatible TCV infection.[18] Whether nuclear CP similarly controls host responses and disease during compatible infection of susceptible *Arabidopsis*, however, has remained unclear.

Salicylic acid (SA) is broadly associated with antiviral defense and is required for efficient HRT-mediated resistance to TCV.[19-21] However, the relationship between SA signaling and disease during compatible TCV infection is less straightforward. Increased SA does not confer TCV resistance in susceptible Col-0 plants,[19] and the N-terminal CP mutant R6A causes more severe disease than WT TCV while also appearing to alter SA-dependent basal immunity.[22] These observations raise the possibility that SA may contribute directly to disease severity during susceptible TCV infection and that CP may influence the magnitude of this response.

Here, we initially tested whether nuclear accumulation of TCV CP is required for TCV pathogenesis in the susceptible Col-0 background of *Arabidopsis*. We re-directed CP away from the nucleus using an identical nuclear export signal (NES) positioned at either the N- or C-terminus. Although both constructs substantially reduced nuclear CP accumulation, they produced opposite effects on symptoms, viral accumulation, particle formation, and host transcriptional responses. These observations redirected the study from CP localization toward the broader question of how different CP configurations affect infection outcomes. Using transcriptomics and functional analysis of SA-associated responses, we show that SA is a major determinant of TCV-associated disease but is not a simple predictor of viral fitness. Instead, the functional state of CP

determines both the magnitude of the SA-associated host response and whether SA supports or restricts viral accumulation.

Results

Nuclear CP accumulation is dispensable for TCV pathogenesis, assembly, and HRT recognition. To determine whether nuclear accumulation of TCV CP contributes to pathogenesis, we appended an identical nuclear export signal (NES) to either the N or C terminus of CP in infectious TCV clones, generating N-NES and C-NES, respectively (**Fig. 1A**). Immunolocalization in infected roots confirmed that both modifications effectively depleted CP from nuclei (**Fig. 1B**). Despite similar CP localization, the two viruses produced strikingly different infection outcomes. N-NES caused enhanced chlorosis and more severe disease and accumulated to significantly higher levels than WT TCV at 14 dpi (**Fig. 1C-E**). In contrast, C-NES caused markedly attenuated symptoms and accumulated at substantially lower levels. These findings demonstrate that sustained nuclear CP accumulation is not required for severe TCV disease and that the attenuation of C-NES cannot be attributed solely to nuclear exclusion.

We next asked whether the divergent infection phenotypes reflected loss of a conserved nonstructural CP activity. WT, N-NES, and C-NES CPs each retained viral suppressor of RNA silencing (VSR) activity in transient assays in *N. benthamiana* (**Fig. 1F,G**), indicating that neither terminal fusion abolished VSR activity. In contrast, ultrastructural analysis revealed striking differences in virion formation. WT TCV produced electron-dense virions, N-NES produced smaller capsid-like particles with

morphology consistent with reduced genomic RNA content or poor encapsidation,[23,24] while no virions were detected during C-NES infection (**Fig. 1H**). Virion protection assays further supported the TEM results. Sap collected from systemically-infected plants was incubated at 37°C to enhance endogenous RNase activity, followed by RT-qPCR quantification of viral RNA. Despite its higher total virus accumulation, N-NES exhibited a >10-fold reduction in RNase-protected viral RNA, while C-NES RNA was undetectable (**Fig. 1I**). Consistent with these differences, 37°C-treated sap from WT TCV- and N-NES-infected plants retained infectivity in Col-0, as evidenced by symptom development and detection of CP in systemic leaves, whereas 37°C-treated C-NES sap failed to establish infection (**Fig. 1J**). These results indicate that terminal modification does not uniformly inactivate CP but instead disrupts distinct stages of virion formation. N-terminal modification permits capsid formation but compromises genome incorporation, whereas C-terminal modification prevents detectable capsid formation. These phenotypes are consistent with previous biochemical and virus-like particle studies implicating the N-terminal R domain in RNA binding and encapsidation and the C-terminal P domain in particle assembly.[24]

Previous transient-expression studies in *N. benthamiana* proposed that nuclear accumulation of TCV CP contributes to HRT-mediated recognition and HR-associated necrosis.[18] We therefore tested whether this relationship was maintained during infection of resistant Di-17 *Arabidopsis*. WT TCV and C-NES elicited a clear HR, whereas N-NES did not (**Fig. 1K**). This loss of HR during N-NES infection, is consistent with previous findings that perturbation of the CP N terminus, including the R6A mutation, disrupts HRT-mediated recognition in Di-17.[22] More recently, an N-terminal

YFP-CP fusion was similarly shown to prevent HRT-dependent HR in transient assays.[25] Consistent with its failure to elicit HR, N-NES was also the only virus to produce appreciable disease symptoms in Di-17 plants by 14 dpi (**Fig. 1L**). Tissue prints of systemic leaves collected at 14 dpi further detected CP only in N-NES-infected plants, indicating that loss of HRT-mediated recognition permitted systemic infection. Importantly, the contrasting HR phenotypes of C-NES and N-NES, despite a similar depletion of nuclear CP, demonstrate that sustained nuclear CP accumulation is not required for HRT-mediated HR during TCV infection as previously proposed.[18]

TCV CP variants differentially activate an SA-associated host response. To further investigate how CP variants influence the host response in susceptible *Arabidopsis*, transcriptome profiling (RNA-seq) was performed on WT, N-NES, and C-NES-infected Col-0 at 14 dpi. WT and N-NES infections produced broadly similar transcriptional profiles and clustered together relative to C-NES and mock-treated plants (**Fig. 2A**). Pairwise comparison of each virus with mock-infected plants revealed substantial overlap among differentially expressed genes (DEGs), although the magnitude of the transcriptional response differed considerably between viruses. C-NES induced the fewest DEGs, followed by WT TCV, whereas N-NES produced the largest transcriptional response (**Fig. 2B, Data S1**). Despite these differences, all three viruses activated a shared defense-associated gene set that included *AGO1*, *AGO2*, and *DRB4* which have each been implicated in antiviral defense against TCV in *Arabidopsis* (**Fig. 2B**).[26,27] These results suggest that the attenuated response to C-NES did not reflect a general failure to activate antiviral defense.

Hierarchical clustering of the 2,000 most variable transcripts further separated the infection states, with WT TCV and N-NES exhibiting similar expression profiles that were distinct from Mock and C-NES (**Fig. 2C, Data S2**). Genes coordinately downregulated by WT and N-NES (Cluster 1) were enriched for photosynthesis-associated processes, while genes preferentially induced by WT and N-NES (Cluster 2) were enriched for cellular processes including systemic acquired resistance, senescence, and response to SA (**Fig. 2C**). To further assess SA-associated defense activation, we examined a panel of representative SA-associated defense genes, including the canonical SA-responsive marker *PR1*,[28] the key SA-signaling regulators *NPR1* and *NPR3*,[29,30] and transcriptional regulators of SA biosynthesis and defense, including *CBP60G*, *SARD1*,[31] and multiple *WRKY* family members,[32] some of which have been implicated in TCV defense.[21,33] WT and N-NES strongly induced this gene set, whereas induction was markedly attenuated during C-NES infection (**Fig. 2D**). The strong induction of SA-associated defense genes in WT and N-NES prompted direct quantification of free SA using an *Acinetobacter* sp. biosensor.[34] WT TCV induced substantial SA accumulation relative to mock, which was further elevated during N-NES infection, whereas C-NES induced only a modest increase above Mock (**Fig. 2E**). Independent measurement of *PR1* expression recapitulated this pattern, with strong induction by WT and N-NES but only minimal induction by C-NES (**Fig. 2F**). Together, these results identify SA accumulation and SA-associated gene expression as major factors distinguishing the infection states produced by CP variants. Importantly, SA accumulation closely tracked disease severity, increasing with N-NES and remaining low with the attenuated C-NES infection. This relationship prompted us to test whether

SA is merely a marker of disease severity or instead contributes directly to disease development and viral accumulation during TCV infection.

Salicylic acid drives TCV-associated disease but has CP-dependent effects on viral accumulation. To determine whether SA contributes causally to the disease phenotypes associated with the different CP variants, WT, N-NES, and C-NES infections were followed for 28 days in Col-0 and the SA-deficient *sid2-2* mutant (**Fig. 3A**). Quantitative image segmentation of healthy, chlorotic, and necrotic tissue demonstrated markedly reduced disease progression in *sid2-2*, compared with Col-0, for all three viruses (**Fig. 3A,B**). Thus, regardless of their differences in accumulation or CP configuration, SA is a major driver of the chlorosis and tissue damage associated with TCV infection in the Col-0 background.

The effects of SA on viral accumulation, however, were strikingly genotype dependent. WT and N-NES accumulated less efficiently in *sid2-2* than in Col-0 suggesting that SA counterintuitively promotes accumulation of these viruses (**Fig. 3C**). In support of this, exogenous SA supplied by foliar application and soil drench restored both WT and N-NES accumulation in *sid2-2* to Col-0 levels (**Fig. 3C**). In contrast, C-NES accumulation was not reduced in *sid2-2* relative to Col-0 and rather than increasing C-NES accumulation, exogenous SA treatment of *sid2-2* further suppressed accumulation of the C-terminal mutant. Together, these results indicate that SA's effect on TCV accumulation is determined by CP context, promoting WT and N-NES while restricting C-NES.

An N-terminal CP mutation uncouples SA-dependent disease from viral accumulation. The preceding experiments demonstrated that SA promotes TCV-

associated disease but has different effects on viral accumulation depending on CP configuration. To further examine this relationship, we turned to the previously characterized CP mutant R6A, an N-terminal substitution that causes more severe disease than WT TCV, although its effects on viral accumulation appeared to vary with infection stage.[22,35] We therefore used R6A to test whether enhanced disease severity could be uncoupled from viral accumulation and whether this phenotype was associated with increased SA accumulation. Additionally, to determine if modification of the C-terminus could influence the R6A phenotype, we generated R6A$^{C\text{-}NES}$, a double mutant containing the N-terminal R6A substitution and the C-terminal NES fusion. We compared disease development, SA accumulation, and viral accumulation during WT, R6A, and R6A$^{C\text{-}NES}$ infection. R6A produced substantially more severe disease than WT TCV over a 28-day infection time course in Col-0 plants with chlorotic and necrotic tissue comprising ~40% of all plant tissue at 14 dpi (**Fig. 4A,B**). However, this phenotype was reversed by addition of the C-terminal NES to R6A, which drastically reduced symptom development (**Fig. 4A,B**). Consistent with these phenotypes, R6A induced significantly greater SA accumulation than WT TCV, whereas addition of the C-NES nearly eliminated SA accumulation and markedly reduced expression of the SA-responsive marker *PR1* compared with WT TCV and R6A infection (**Fig. 4C,D**). The severe R6A phenotype was strongly dependent on SA biosynthesis, as R6A-induced disease was markedly attenuated in *sid2-2* relative to Col-0 beginning at 14 dpi (**Fig. 4E,F**). Importantly, this enhanced disease and increased SA accumulation, did not reflect increased viral accumulation. RT-qPCR showed that R6A accumulated to significantly lower levels than WT TCV in Col-0 at 14 dpi, whereas accumulation was

indistinguishable in the *sid2-2* background (**Fig. 4G**). Thus, elevated SA during R6A infection is uncoupled from viral accumulation, demonstrating that SA is not simply a consequence of increased viral burden. Moreover, the failure of R6A to lose accumulation in *sid2-2* suggests that the R6 residue is likely required for TCV to benefit from an SA-rich host environment. Similar to the relationship between TCV and C-NES, R6A$^{C\text{-}NES}$ accumulation remained significantly reduced relative to R6A in both Col-0 and *sid2-2* plants (**Fig. 4G**).

To determine how the distinct infection states were reflected at the transcriptome level, we compared gene-expression profiles across the CP variants and SA-deficient backgrounds. PCA revealed a clear progression along PC1, which accounted for more than 50% of the transcriptional variance (**Fig. 4H**). Across PC1, infection conditions were broadly distributed according to SA accumulation and disease severity. R6A and N-NES clustered at one extreme, corresponding to the highest SA accumulation and most severe disease, whereas mock-infected plants occupied the opposite extreme (**Fig. 4H**). Notably, R6A produced one of the strongest transcriptomic shifts despite accumulating to lower levels than WT TCV. Together, these data demonstrate that the magnitude of host transcriptional response during TCV infection is closely associated with SA accumulation and disease severity rather than with viral RNA abundance alone. Together, CP emerges as a key determinant of both SA induction during TCV infection and whether that SA-rich environment ultimately favors or restricts viral accumulation.

Discussion

We initially sought to determine whether nuclear accumulation of CP was required for TCV pathogenesis by directing CP away from the nucleus with an identical NES positioned at either terminus. Instead, the two constructs produced opposite infection phenotypes despite similarly reducing nuclear CP accumulation. A role for nuclear CP in HRT-dependent immunity has been proposed primarily from transient-expression assays, in which exclusion of CP from the nucleus was associated with reduced HRT-dependent cell death.[18] Separately, mutations within the CP N terminus, including R6A, can evade HR in resistant Di-17 plants,[22] establishing this region of CP as an important determinant of HRT-mediated recognition but not directly linking that recognition to CP nuclear localization. Our infection data distinguish these two phenomena. C-NES retained the ability to elicit a robust HR in Di-17 despite strong depletion of CP from nuclei, indicating that sustained nuclear CP accumulation is not required for HRT-mediated recognition during TCV infection. In contrast, N-NES failed to elicit HR, phenocopying the previously characterized R6A escape phenotype and suggests that perturbation of the CP N terminus disrupts HRT recognition. The same positional dependence was also evident in susceptible Col-0 plants, where the two NES constructs produced sharply different SA and disease phenotypes. N-NES induced elevated SA accumulation and more severe disease than WT TCV, whereas C-NES induced little SA and caused markedly attenuated symptoms. This close correspondence between SA levels and symptom severity suggested that SA is a major determinant of disease severity during TCV infection.

Previous work showed that TCV particle formation contributes to efficient movement from the vasculature into systemic leaves.[13] Interestingly, N-NES accumulated to higher levels than WT TCV in systemic tissue despite producing virions with poorly encapsidated RNA. Thus, only a relatively small population of properly formed particles may be sufficient to support systemic movement. Alternatively, reduced encapsidation could contribute to the increased total RNA accumulation of N-NES by leaving a larger pool of viral RNA available for replication rather than packaging. These possibilities could explain how N-NES accumulates abundant viral RNA in systemic tissue despite inefficient production of mature virions. Notably, C-NES failed to form detectable virions and induced only weak SA, whereas both WT and N-NES formed intact particles and strongly activated SA. This pattern raises the possibility that formation of an intact virion is a major determinant of SA accumulation during TCV infection.

The *sid2-2* experiments establish SA as a causal driver of TCV-associated disease. Across WT, N-NES, and C-NES infections, loss of normal SA biosynthesis delayed and reduced chlorosis and necrosis over the 28-day time course. In Col-0 plants, disease severity did not simply reflect viral accumulation. R6A caused more severe disease than WT despite accumulating less viral RNA, indicating that tissue damage tracked SA accumulation more closely than viral load. Unexpectedly, SA did not exert a uniform effect on viral RNA accumulation. WT and N-NES accumulated less efficiently in *sid2-2*, and exogenous SA restored their accumulation, demonstrating that SA makes a positive net contribution to these infections under the conditions examined. Conversely, C-NES accumulation was unchanged in *sid2-2* plants relative to Col-0 and

the addition of exogenous SA restricted its accumulation, suggesting that C-NES is unable to benefit from SA. Thus, SA broadly promoted TCV-associated disease, but its effect on viral accumulation could be either pro- or antiviral depending on CP configuration. One possibility is that WT and N-NES retain CP functions that permit them to tolerate antiviral SA outputs while benefiting from other SA-dependent changes in the cellular environment. In contrast, C-NES induces little SA accumulation and is restricted when challenged with an exogenous SA treatment. These findings suggest that modifications to the CP termini not only influence the magnitude of SA induction, but also the capacity of TCV to benefit from SA or SA-associated outputs.

Together, these findings support a model in which a viral structural protein determines not only the magnitude of the host immune response but also its consequences for infection. TCV CP appears to enable certain viral states to tolerate or exploit an SA-rich host environment, whereas other CP states remain susceptible to the antiviral effects of SA. These findings improve our understanding of how SA can promote disease while having opposing effects on viral accumulation.

Materials and Methods

Plant materials, growth conditions, and virus construction and infection. *Arabidopsis thaliana* Col-0 (CS70000) and *sid2-2* (CS16438) were obtained from the Arabidopsis Biological Resource Center (ABRC) while the Di-17 ecotype was a generous gift from Dr. Pradeep Kachroo (University of Kentucky). All plants (including *N. benthamiana* LAB strain) were grown and maintained in plant growth chambers (Caron Scientific, Marietta, Ohio) with the following conditions: 12/12 hr light/dark, LED lights

set at 200 µmol $m^{-2}s^{-1}$ intensity, 25°C, and 65% humidity. TCV isolate M (GenBank: PX830476) was used for this study.[36] and was used as a template for site-directed mutagenesis (SDM) to append the pyruvate kinase NES to the N or C terminus of CP in full-length TCV to create N-NES and C-NES, respectively. Additionally, full-length TCV was used to introduce the previously described R6A point mutation with or without the C-NES mutation into CP. Resulting clones were sequenced using whole plasmid sequencing (Plasmidsaurus) to verify cloning accuracy. SDM primers are listed in Table S1.

Four-week-old *A. thaliana* plants were selected and grouped for experiments based on size. Full-length TCV plasmids were linearized with *Sma*I overnight at 25°C. TCV RNAs were synthesized using HiScribe® T7 Quick High Yield RNA Synthesis Kit (New England Biolabs) per the manufacturers protocol. Silicon carbide powder was applied to two rosette leaves per plant and 1 µg RNA or 5 µL H_2O (mock-infected plants) was gently rubbed on selected leaves. For exogenous SA treatments, plants were sub-irrigated with 500 µM SA at 24 hours post-infection and subsequently sprayed with 500 µM SA every 48 hours. Systemic leaves were harvested for downstream analysis at 14-days post-infection (dpi) unless otherwise noted.

Virus accumulation, silencing suppression, and virion analysis. Systemically infected leaves were harvested and stored at -80°C prior to processing. Samples were pulverized in liquid nitrogen, resuspended in TRIzol (Thermo Scientific), and RNA was extracted following the manufacturers protocol. After extraction, an RQ1 DNase digest was performed (Promega, Madison, Wisconsin) according to the manufacturers protocol to remove residual DNA. One-step reverse-transcription quantitative PCR (RT-qPCR)

was performed using approximately 20 ng of purified RNA and the SYBR Green-based Luna® Universal One-Step RT-qPCR kit (New England BioLabs) per manufacturers protocol with reaction volumes reduced to 10 μL. Samples were analyzed using a BioRad CFX Connect Real-Time PCR detection system with CFX Maestro software. Primer sequences used in this study are available in Table S1.

To measure VSR activity, 16c *N. benthamiana* plants expressing a GFP transgene,[37] were agroinfiltrated with either GFP alone, or alongside the p14 VSR,[38] Myc:CP, Myc:CP$^{N\text{-}NES}$, or Myc:CP$^{C\text{-}NES}$. At 5 dpi, whole leaves were imaged for GFP fluorescence using an Azure 600 Imaging System (Azure Biosystems). Infiltrated spots were harvested for western blotting or RNA purification and RT-qPCR using primers targeting GFP or ubiquitin (reference gene).

For transmission electron microscopy, sap from systemically infected leaves was collected at 14 dpi. Negative staining and imaging of sap was performed by the Electron Microscopy Research Laboratory (EMRL) at the University of Kansas Medical Center (Kansas City, KS) To quantitate RNase-protected viral RNA, sap was collected from systemically infected leaves and heated to 37°C for 30 minutes to activate endogenous RNase activity.[39] RNA was then purified using TRIzol followed by RT-qPCR as described above. Cq values were converted to TCV RNA copies/μL of sap using a standard curve generated from RT-qPCR of known concentrations of the full-length TCV plasmid. To assess infectivity, heat-treated sap was subsequently used to inoculate naive Col-0 plants.

Plant imaging, immunolocalization, and western blotting. Chlorotic and necrotic regions were quantified from RGB plant images using a threshold-based workflow in

ImageJ/Fiji (TWS pipeline) coupled to supervised pixel classification. Whole plants were segmented and analyzed using a trained classifier to assign each plant pixel to one of three tissue classes: healthy (green), yellowing (chlorotic), or necrotic.

Immunohistochemistry was performed as previously described with modifications.[40] *Arabidopsis* roots were harvested at 14 dpi, rinsed, and incubated in fixation solution (4% paraformaldehyde, 50 mM HEPES pH 7.5, 1 mM $MgCl_2$) for 30 minutes at room temperature. Roots were then washed in 1X TBST and incubated in blocking buffer (3% BSA in 1X TBST) for 1-2 hours at room temperature before incubation in primary rabbit anti-CP (1:10,000 dilution; manufactured by Sino Biological, Paoli, PA) overnight at 4°C. Roots were washed in 1X TBST, incubated in the secondary antibody, Alexa-488 conjugated goat anti-rabbit (1:2,000 dilution; Abcam Cat#:AB1500777), for 1-2 hours at room temperature, washed, and submerged in DAPI for 10 minutes to stain nuclei. Roots were mounted and imaged with confocal microscopy at 40X magnification.

For western blotting, leaf samples were pulverized with liquid nitrogen, resuspended in 1X TBS + 3% β-mercaptoethanol supplemented with protease inhibitor cocktail (Thermo Scientific, Waltham, Massachusetts), mixed with Laemmli buffer and boiled at 95°C for 5-10 min. Proteins were separated using SDS-PAGE and transferred to nitrocellulose membrane using the Bio-Rad Trans-Blot Semi-Dry Transfer system. Membranes were stained with Ponceau S (0.2% w/v) to detect the Rubisco large subunit for loading controls. Following blocking in 1X TBS + 0.1% Tween 20, 3% bovine serum albumin, primary rabbit anti-CP (manufactured by Sino Biological) antibodies at a 1:10,000 dilution were added and incubated at 4°C overnight. Following secondary

antibody incubation (Thermo Scientific Pierce Goat Anti-Rabbit IgG Peroxidase Conjugated at 1:10,000 dilution), proteins were detected using SuperSignal West Pico PLUS Chemiluminescent Substrate (Thermo Scientific) per manufacturer's protocol. Blots were imaged using an Azure 600 Imaging System (Azure Biosystems, Dublin, CA).

For tissue printing, the abaxial surfaces of systemic leaves were pressed onto nitrocellulose membranes, and color images of the leaves were captured as loading references. Membranes were washed with 1X TBST, blocked with Western blot blocking buffer, and incubated with anti-CP primary antibody (1:10,000 in blocking buffer). After washing, membranes were incubated in anti-rabbit secondary antibody (1:10,000 in blocking buffer), exposed to the SuperSignal West Pico PLUS Chemisluminescent substrate, and imaged as described above for Western blotting.

Salicylic acid quantification. Acinetobacter ADPWH_*lux*[34] was a generous gift from Dr. Denise Pallett (UK Centre for Ecology and Hydrology) and free SA was quantified as previously described.[41] Reactions were carried out in a 96-well plate and luminescence was detected using the BioTek Synergy Neo2 hybrid multimode microplate reader (Agilent Technologies, Santa Clara, CA) and the BioTek Gen6 1.04 software. For each experiment, a standard curve was generated using *sid2-2* lysates spiked with known amounts of SA (0, 10, 25, 50, 100, and 200 ng). Luminescence measurements were imported into GraphPad Prism, where a standard curve was fitted and used to interpolate experimental sample concentrations of free SA.

RNA sequencing and bioinformatic analyses. Trizol-purified total RNAs were used to construct Poly(A)-enriched RNA-seq libraries that were sequenced as 3′-tag

single-end libraries on an Illumina platform (Plasmidsaurus; ~20 million raw reads and ~10 million deduplicated 3′ end counting reads per sample). Raw reads were subjected to quality control and adapter/quality trimming with fastp[42] (v0.24.0) prior to quantification, and only filtered, high-quality reads were used for alignment to the *A. thaliana* TAIR10 reference genome using STAR[43] (v2.7.11). PCR and optical duplicates were eliminated via UMI-guided deduplication using UMIcollapse[44] (v1.1.0). Gene-level expression was quantified with featureCounts[45] (Subread v2.1.1). Raw count matrices were analyzed in iDEP[46] (v2.01) for PCA, differential expression testing using DESeq2, hierarchical clustering, and Gene Ontology (GO) biological process analyses. To generate dendograms, raw RNA-seq were normalized to counts per million (CPM) and $\log_2$-transformed. Lowly expressed genes (counts <10) were excluded from the analysis, and normalized expression values from three biological replicates were averaged for each experimental condition. Pairwise distances between conditions were calculated using Pearson correlation distance (1-r), and hierarchical clustering was performed using the average-linkage method.

Acknowledgements

We thank Roy Pescador of the Electron Microscopy Research Laboratory at the University of Kansas Medical Center for technical assistance with transmission electron microscopy (TEM). We also thank Dr. Sven-Erik Behrens of Martin Luther University Halle-Wittenberg for generously providing purified protein used to generate the antibodies used in this study. This research was supported by the National Institute of General Medical Sciences (NIGMS) of the National Institutes of Health (NIH) under award R35GM154909 to J.P.M.

Author contributions

Dana J. Rademacher: Conceptualization, Investigation, Formal Analysis, Methodology, Visualization, Writing – review & editing; **Braeden Kingsolver:** Investigation; **Akashata Dawane:** Investigation; **Jared P. May:** Conceptualization, Data Curation, Formal Analysis, Funding Acquisition, Visualization, Writing – original draft, Writing – review & editing, Resources, and Supervision

Declaration of interests

The authors declare no competing interests.

Declaration of generative AI and AI-assisted technologies in the writing process

Generative artificial intelligence (ChatGPT) was used during manuscript preparation solely to support language refinement, including grammar, clarity, and correction of typographical errors. All AI-assisted edits were reviewed and revised by the authors, who assume full responsibility for the final manuscript content.

Supplemental Information

Data S1: DESeq2 results for virus infections (TCV, N-NES, or C-NES) vs. Mock
Data S2: DESeq2 results for top 2000 genes for hierarchical clustering
Table S1: List of primers used in this study

References

1 Ivanov, K. I. & Mäkinen, K. Coat proteins, host factors and plant viral replication. *Curr Opin Virol* **2**, 712-718, doi:10.1016/j.coviro.2012.10.001 (2012).

2 Tenllado, F. & Bol, J. F. Genetic dissection of the multiple functions of alfalfa mosaic virus coat protein in viral RNA replication, encapsidation, and movement. *Virology* **268**, 29-40, doi:10.1006/viro.1999.0170 (2000).
3 Qu, F., Ren, T. & Morris, T. J. The Coat Protein of Turnip Crinkle Virus Suppresses Posttranscriptional Gene Silencing at an Early Initiation Step. *Journal of Virology* **77**, 511-522, doi:10.1128/jvi.77.1.511-522.2003 (2003).
4 Bendahmane, A., Köhn, B. A., Dedi, C. & Baulcombe, D. C. The coat protein of potato virus X is a strain-specific elicitor of Rx1-mediated virus resistance in potato. *Plant J* **8**, 933-941, doi:10.1046/j.1365-313x.1995.8060933.x (1995).
5 Gao, Z. *et al.* Coat proteins of necroviruses target 14-3-3a to subvert MAPKKKα-mediated antiviral immunity in plants. *Nat Commun* **13**, 716, doi:10.1038/s41467-022-28395-5 (2022).
6 Han, K. *et al.* Pepper mild mottle virus coat protein interacts with pepper chloroplast outer envelope membrane protein OMP24 to inhibit antiviral immunity in plants. *Horticulture Research* **10**, doi:10.1093/hr/uhad046 (2023).
7 Taliansky, M. E., Brown, J. W., Rajamäki, M. L., Valkonen, J. P. & Kalinina, N. O. Involvement of the plant nucleolus in virus and viroid infections: parallels with animal pathosystems. *Adv Virus Res* **77**, 119-158, doi:10.1016/b978-0-12-385034-8.00005-3 (2010).
8 Herranz, M. C., Pallas, V. & Aparicio, F. Multifunctional roles for the N-terminal basic motif of Alfalfa mosaic virus coat protein: nucleolar/cytoplasmic shuttling, modulation of RNA-binding activity, and virion formation. *Mol Plant Microbe Interact* **25**, 1093-1103, doi:10.1094/mpmi-04-12-0079-r (2012).
9 Callaway, A., Giesman-Cookmeyer, D., Gillock, E. T., Sit, T. L. & Lommel, S. A. THE MULTIFUNCTIONAL CAPSID PROTEINS. *Annual Review of Phytopathology* **39**, 419-460, doi:https://doi.org/10.1146/annurev.phyto.39.1.419 (2001).
10 Ivanov, K. I., Puustinen, P., Merits, A., Saarma, M. & Mäkinen, K. Phosphorylation down-regulates the RNA binding function of the coat protein of potato virus A. *J Biol Chem* **276**, 13530-13540, doi:10.1074/jbc.M009551200 (2001).
11 Bakker, S. E. *et al.* Isolation of an asymmetric RNA uncoating intermediate for a single-stranded RNA plant virus. *J Mol Biol* **417**, 65-78, doi:10.1016/j.jmb.2012.01.017 (2012).
12 Hogle, J. M., Maeda, A. & Harrison, S. C. Structure and assembly of turnip crinkle virus: I. X-ray crystallographic structure analysis at 3.2 Å resolution. *Journal of Molecular Biology* **191**, 625-638, doi:https://doi.org/10.1016/0022-2836(86)90450-X (1986).
13 Cao, M. *et al.* The capsid protein of Turnip crinkle virus overcomes two separate defense barriers to facilitate systemic movement of the virus in Arabidopsis. *J Virol* **84**, 7793-7802, doi:10.1128/jvi.02643-09 (2010).
14 Thomas, C. L., Leh, V., Lederer, C. & Maule, A. J. Turnip crinkle virus coat protein mediates suppression of RNA silencing in Nicotiana benthamiana. *Virology* **306**, 33-41, doi:10.1016/s0042-6822(02)00018-1 (2003).
15 Dempsey, D. A., Pathirana, M. S., Wobbe, K. K. & Klessig, D. F. Identification of an Arabidopsis locus required for resistance to turnip crinkle virus. *Plant J* **11**, 301-311, doi:10.1046/j.1365-313x.1997.11020301.x (1997).

16 Zhao, Y. *et al.* The amino terminus of the coat protein of Turnip crinkle virus is the AVR factor recognized by resistant arabidopsis. *Mol Plant Microbe Interact* **13**, 1015-1018, doi:10.1094/mpmi.2000.13.9.1015 (2000).
17 Ren, T., Qu, F. & Morris, T. J. HRT gene function requires interaction between a NAC protein and viral capsid protein to confer resistance to turnip crinkle virus. *Plant Cell* **12**, 1917-1926, doi:10.1105/tpc.12.10.1917 (2000).
18 Kang, S. H., Qu, F. & Morris, T. J. A nuclear fraction of turnip crinkle virus capsid protein is important for elicitation of the host resistance response. *Virus Res* **210**, 264-270, doi:10.1016/j.virusres.2015.08.014 (2015).
19 Kachroo, P., Yoshioka, K., Shah, J., Dooner, H. K. & Klessig, D. F. Resistance to turnip crinkle virus in Arabidopsis is regulated by two host genes and is salicylic acid dependent but NPR1, ethylene, and jasmonate independent. *Plant Cell* **12**, 677-690, doi:10.1105/tpc.12.5.677 (2000).
20 Singh, D. P., Moore, C. A., Gilliland, A. & Carr, J. P. Activation of multiple antiviral defence mechanisms by salicylic acid. *Mol Plant Pathol* **5**, 57-63, doi:10.1111/j.1364-3703.2004.00203.x (2004).
21 Chandra-Shekara, A. C. *et al.* Light-dependent hypersensitive response and resistance signaling against Turnip Crinkle Virus in Arabidopsis. *Plant J* **45**, 320-334, doi:10.1111/j.1365-313X.2005.02618.x (2006).
22 Donze, T., Qu, F., Twigg, P. & Morris, T. J. Turnip crinkle virus coat protein inhibits the basal immune response to virus invasion in Arabidopsis by binding to the NAC transcription factor TIP. *Virology* **449**, 207-214, doi:https://doi.org/10.1016/j.virol.2013.11.018 (2014).
23 Hesketh, E. L., Meshcheriakova, Y., Thompson, R. F., Lomonossoff, G. P. & Ranson, N. A. The structures of a naturally empty cowpea mosaic virus particle and its genome-containing counterpart by cryo-electron microscopy. *Scientific Reports* **7**, 539, doi:10.1038/s41598-017-00533-w (2017).
24 Saunders, K. & Lomonossoff, G. P. The Generation of Turnip Crinkle Virus-Like Particles in Plants by the Transient Expression of Wild-Type and Modified Forms of Its Coat Protein. *Front Plant Sci* **6**, 1138, doi:10.3389/fpls.2015.01138 (2015).
25 Jo, S. H. *et al.* Functional Dissection of the Turnip Crinkle Virus Coat Protein Links ATG8 Association to Autophagy-Associated Antiviral Regulation. *Molecular Plant Pathology* **27**, e70350, doi:https://doi.org/10.1111/mpp.70350 (2026).
26 Qu, F., Ye, X. & Morris, T. J. Arabidopsis DRB4, AGO1, AGO7, and RDR6 participate in a DCL4-initiated antiviral RNA silencing pathway negatively regulated by DCL1. *Proceedings of the National Academy of Sciences* **105**, 14732-14737, doi:doi:10.1073/pnas.0805760105 (2008).
27 Harvey, J. J. *et al.* An antiviral defense role of AGO2 in plants. *PLoS One* **6**, e14639, doi:10.1371/journal.pone.0014639 (2011).
28 Lebel, E. *et al.* Functional analysis of regulatory sequences controllingPR-1 gene expression in Arabidopsis. *The Plant Journal* **16**, 223-233, doi:https://doi.org/10.1046/j.1365-313x.1998.00288.x (1998).
29 Wu, Y. *et al.* The Arabidopsis NPR1 protein is a receptor for the plant defense hormone salicylic acid. *Cell Rep* **1**, 639-647, doi:10.1016/j.celrep.2012.05.008 (2012).

30 Fu, Z. Q. *et al.* NPR3 and NPR4 are receptors for the immune signal salicylic acid in plants. *Nature* **486**, 228-232, doi:10.1038/nature11162 (2012).
31 Wang, L. *et al.* CBP60g and SARD1 play partially redundant critical roles in salicylic acid signaling. *Plant J* **67**, 1029-1041, doi:10.1111/j.1365-313X.2011.04655.x (2011).
32 Peng, Y., Yang, J., Li, X. & Zhang, Y. Salicylic Acid: Biosynthesis and Signaling. *Annual Review of Plant Biology* **72**, 761-791, doi:https://doi.org/10.1146/annurev-arplant-081320-092855 (2021).
33 Gao, R., Liu, P., Yong, Y. & Wong, S. M. Genome-wide transcriptomic analysis reveals correlation between higher WRKY61 expression and reduced symptom severity in Turnip crinkle virus infected Arabidopsis thaliana. *Sci Rep* **6**, 24604, doi:10.1038/srep24604 (2016).
34 Huang, W. E. *et al.* Chromosomally located gene fusions constructed in Acinetobacter sp. ADP1 for the detection of salicylate. *Environ Microbiol* **7**, 1339-1348, doi:10.1111/j.1462-5822.2005.00821.x (2005).
35 Kang, S.-H., Qu, F. & Morris, T. J. A spectrum of HRT-dependent hypersensitive responses elicited by the 52 amino acid N-terminus of turnip crinkle virus capsid protein and its mutants. *Virus Research* **200**, 30-34, doi:https://doi.org/10.1016/j.virusres.2015.01.020 (2015).
36 Oh, J. W., Kong, Q., Song, C., Carpenter, C. D. & Simon, A. E. Open reading frames of turnip crinkle virus involved in satellite symptom expression and incompatibility with Arabidopsis thaliana ecotype Dijon. *Mol Plant Microbe Interact* **8**, 979-987, doi:10.1094/mpmi-8-0979 (1995).
37 Ruiz, M. T., Voinnet, O. & Baulcombe, D. C. Initiation and maintenance of virus-induced gene silencing. *Plant Cell* **10**, 937-946, doi:10.1105/tpc.10.6.937 (1998).
38 Mérai, Z. *et al.* Aureusvirus P14 is an efficient RNA silencing suppressor that binds double-stranded RNAs without size specificity. *J Virol* **79**, 7217-7226, doi:10.1128/jvi.79.11.7217-7226.2005 (2005).
39 Qiu, W. & Scholthof, K. B. Genetic identification of multiple biological roles associated with the capsid protein of satellite panicum mosaic virus. *Mol Plant Microbe Interact* **14**, 21-30, doi:10.1094/mpmi.2001.14.1.21 (2001).
40 Durand, C. *et al.* The organization pattern of root border-like cells of Arabidopsis is dependent on cell wall homogalacturonan. *Plant Physiol* **150**, 1411-1421, doi:10.1104/pp.109.136382 (2009).
41 Defraia, C. T., Schmelz, E. A. & Mou, Z. A rapid biosensor-based method for quantification of free and glucose-conjugated salicylic acid. *Plant Methods* **4**, 28, doi:10.1186/1746-4811-4-28 (2008).
42 Chen, S., Zhou, Y., Chen, Y. & Gu, J. fastp: an ultra-fast all-in-one FASTQ preprocessor. *Bioinformatics* **34**, i884-i890, doi:10.1093/bioinformatics/bty560 (2018).
43 Dobin, A. *et al.* STAR: ultrafast universal RNA-seq aligner. *Bioinformatics* **29**, 15-21, doi:10.1093/bioinformatics/bts635 (2013).
44 Liu, D. Algorithms for efficiently collapsing reads with Unique Molecular Identifiers. *PeerJ* **7**, e8275, doi:10.7717/peerj.8275 (2019).

45 Liao, Y., Smyth, G. K. & Shi, W. featureCounts: an efficient general purpose program for assigning sequence reads to genomic features. *Bioinformatics* **30**, 923-930, doi:10.1093/bioinformatics/btt656 (2014).
46 Ge, S. X., Son, E. W. & Yao, R. iDEP: an integrated web application for differential expression and pathway analysis of RNA-Seq data. *BMC Bioinformatics* **19**, 534, doi:10.1186/s12859-018-2486-6 (2018).

Figure 1: Nuclear CP accumulation is dispensable for TCV pathogenesis, assembly, and HRT recognition.
(**A**) Schematic of Turnip crinkle virus variants used in this study. (**B**) Immunohistochemistry of infected Col-0 roots at 14 dpi using anti-CP antibodies with DAPI stain to label nuclei. (**C**) Infected Col-0 plants at 14 dpi. Disease symptoms are highlighted using a trainable segmentation analysis in ImageJ (bottom row) separating healthy (green), chlorotic (yellow), and necrotic (red) tissue. (**D**) Percent chlorosis and necrosis of infected Col-0 plants at 14 dpi (n=5). (**E**) TCV accumulation measured by RT-qPCR in Col-0 at 14 dpi (n=5). (**F**) Image of infiltrated *N. benthamiana* 16c leaves at 5 days post-infiltration. Western blot of *N. benthamiana* 16c plants infiltrated with Myc-tagged CP constructs. CP variants present are labeled on the right. Ponceau-S stained Rubisco serves as loading control. (**G**) GFP transcript expression from infiltrated spots was measured by RT-qPCR (n=5). Statistics listed are comparing experimental condition vs. GFP only. (**H**) Transmission electron microscopy with negative staining of infected sap (n=10). (**I**) Relative RNase-protected RNA determined by RT-qPCR (n=5). Values are relative to quantification of WT TCV RNA. (**J**) Col-0 plants at 14 dpi infected with 37°C-treated sap. Tissue print of systemically infected leaves detecting CP. Color images show leaves used in tissue print. Data shown is representative of two independent experiments. (**K**) Local leaves of Di-17 plants at 4 dpi. HR lesions denoted by white arrows. (**L**) Di-17 plants at 14 dpi with corresponding tissue print of systemic leaves detecting CP. Data in panels K and L is representative of two independent experiments. Data in panels D, E, G, and H are representative of the median results across at least two independent experiments. One-way ANOVA with Tukey's multiple comparison was used for all statistical analyses. ****$p<0.0001$

Figure 2: TCV CP variants differentially activate SA-associated host response.
(**A**) Principal component analysis (PCA) of expression profiles of mock or infected Col-0 plants at 14 dpi. Dendogram depicting treatment-level clustering using replicate averaged $\log_2$-CPM expression values. Pairwise distances were calculated as 1-Pearson's correlation coefficient, and hierarchical clustering was performed using average linkage. Branch lengths represent correlation distance. (**B**) Venn diagram of all DEGs identified in virus-infected plants vs Mock. Heat map of defense-associated genes previously implicated in TCV defense. (**C**) Heat-map of hierarchical clustering of the top 2,000 DEGs identified by DESeq2. Gene ontology analysis of biological processes of each cluster identified up-regulated and down-regulated pathways listed to the right. Bar graphs show fold-enrichment and adjusted p-values of selected pathways (**D**) Heat-map of expression of representative SA-responsive genes in infected Col-0 plants. (**E**) Free SA accumulation quantified by *Acinetobacter sp.* ADPWH-lux biosensor (n=5). (**F**) *PR1* expression measured by RT-qPCR (n=5). Data in panels E and F represent the median values across at least two independent experiments. Lognormal one-way ANOVA with Tukey's multiple comparison test was used for statistical analyses.

Figure 3: Salicylic acid drives TCV-associated disease but has CP-dependent effects on viral accumulation.
(**A**) Time-course of infected Col-0 and *sid2-2* plants with corresponding disease image segmentation indicating healthy (green), chlorotic (yellow), and necrotic (red) tissue. (**B**)

Percent healthy tissue of infected whole plants calculated via ImageJ segmentation analysis at indicated time points (n=5). Statistical analysis compares healthy tissue percent between Col-0 (solid dark green line) and *sid2-2* (dashed light green line) plants within each time point tested. Images are representative of plants from at least three independent experiments. (**C**) Virus accumulation measured by RT-qPCR in indicated condition (n=5). Col-0 plants were untreated (solid-colored bars), while *sid2-2* plants were either untreated (-; solid white bars) or treated with salicylic acid (+SA; striped bars) beginning 24 hours post-infection until harvest at 14 dpi. Data in panels B and C represent the median measurements from at least three independent experiments. Lognormal one-way ANOVA with Tukey's multiple comparison used for statistical analysis. *p<0.05 **p<0.01 ****p<0.0001

Figure 4: An N-terminal CP mutation uncouples SA-dependent disease from viral fitness.

(**A**) Time-course of representative Col-0 plants with corresponding disease image segmentation indicating healthy (green), chlorotic (yellow), and necrotic (red) tissue. (**B**) Percent chlorosis and necrosis of infected Col-0 plants at 14 dpi as calculated following ImageJ segmentation (n=5). (**C**) Free SA accumulation quantified by *Acinetobacter sp.* ADPWH-lux biosensor (n=5). (**D**) PR1 expression quantified by RT-qPCR of infected Col-0 at 14 dpi (n=5). (**E**) Time-course of representative *sid2-2* plants with corresponding disease image segmentation. (**F**) Percent healthy tissue of infected Col-0 and *sid2-2* plants calculated following ImageJ segmentation analysis at indicated time points. Statistical analysis compares healthy tissue percent between Col-0 (solid dark green line) and *sid2-2* (dashed light green line) plants within each time point tested (n=5). (**G**) Virus accumulation measured by RT-qPCR at 14 dpi (n=5). (**H**) PCA of gene expression profiles for TCV infections in Col-0 and *sid2-2* plants. Dendrogram depicting treatment-level clustering using replicate averaged $\log_2$-CPM expression values. Red branches indicate severe disease, yellow branches indicate intermediate disease, while green branches indicate uninfected controls. Images in panels A and E are representative of plants from at least three independent experiments. Data in panels B, C, D, F, and G is representative of the median points across at least two independent experiments. Lognormal one-way ANOVA with Tukey's multiple comparison was used for all statistical analyses. **p<0.01 ***p<0.001 ****p<0.0001

Figures

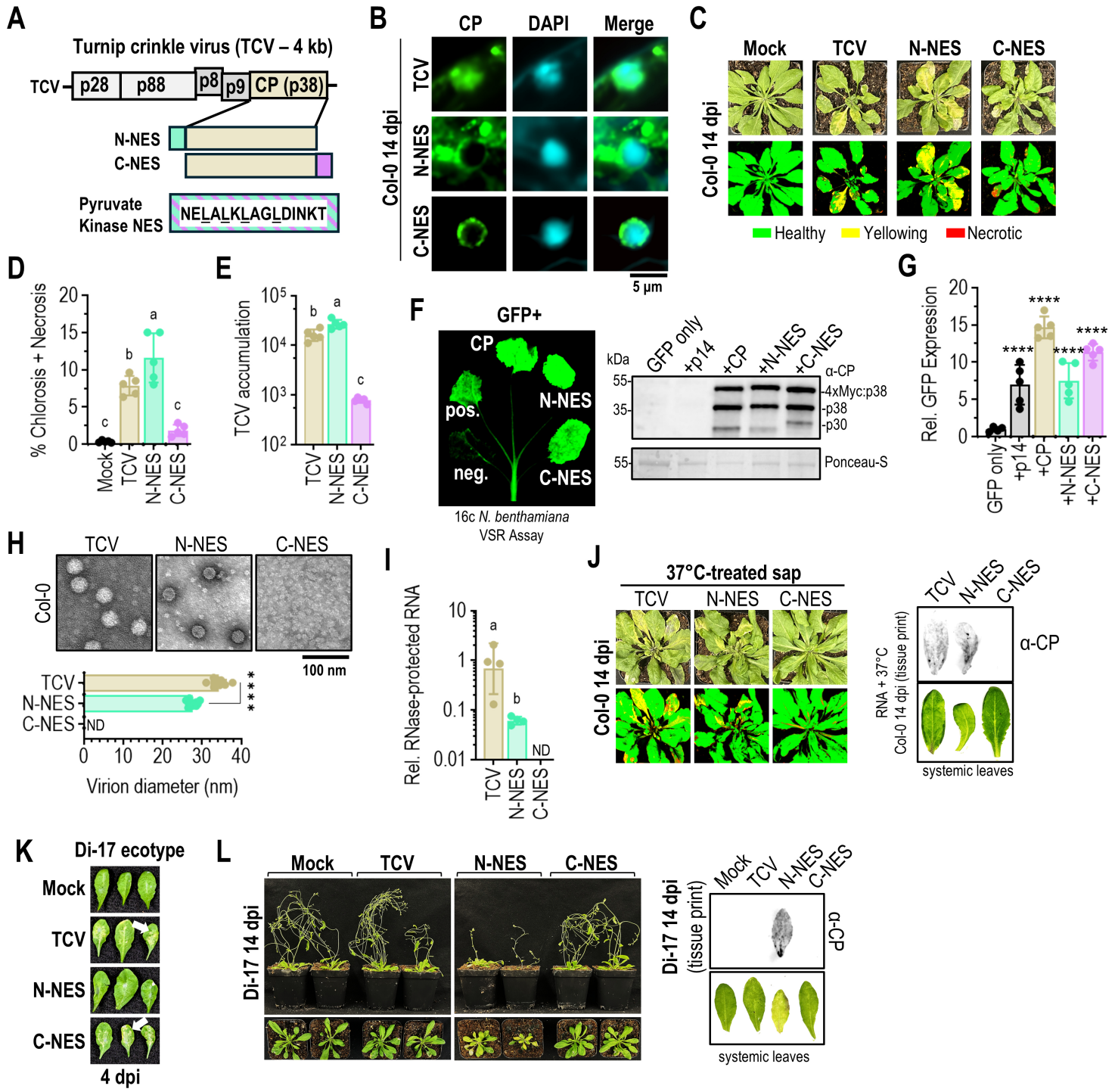


Figure 1

Nuclear CP accumulation is dispensable for TCV pathogenesis, assembly, and HRT recognition.

(A) Schematic of Turnip crinkle virus variants used in this study. (B) Immunohistochemistry of infected Col-0 roots at 14 dpi using anti-CP antibodies with DAPI stain to label nuclei. (C) Infected Col-0 plants at 14 dpi. Disease symptoms are highlighted using a trainable segmentation analysis in ImageJ (bottom

row) separating healthy (green), chlorotic (yellow), and necrotic (red) tissue. (D) Percent chlorosis and necrosis of infected Col-0 plants at 14 dpi (n=5). (E) TCV accumulation measured by RT-qPCR in Col-0 at 14 dpi (n=5). (F) Image of infiltrated N. benthamiana 16c leaves at 5 days post-infiltration. Western blot of N. benthamiana 16c plants infiltrated with Myc-tagged CP constructs. CP variants present are labeled on the right. Ponceau-S stained Rubisco serves as loading control. (G) GFP transcript expression from infiltrated spots was measured by RT-qPCR (n=5). Statistics listed are comparing experimental condition vs. GFP only. (H) Transmission electron microscopy with negative staining of infected sap (n=10). (I) Relative RNase-protected RNA determined by RT-qPCR (n=5). Values are relative to quantification of WT TCV RNA. (J) Col-0 plants at 14 dpi infected with 37°C-treated sap. Tissue print of systemically infected leaves detecting CP. Color images show leaves used in tissue print. Data shown is representative of two independent experiments. (K) Local leaves of Di-17 plants at 4 dpi. HR lesions denoted by white arrows. (L) Di-17 plants at 14 dpi with corresponding tissue print of systemic leaves detecting CP. Data in panels K and L is representative of two independent experiments. Data in panels D, E, G, and H are representative of the median results across at least two independent experiments. One-way ANOVA with Tukey's multiple comparison was used for all statistical analyses. ****$p<0.0001$

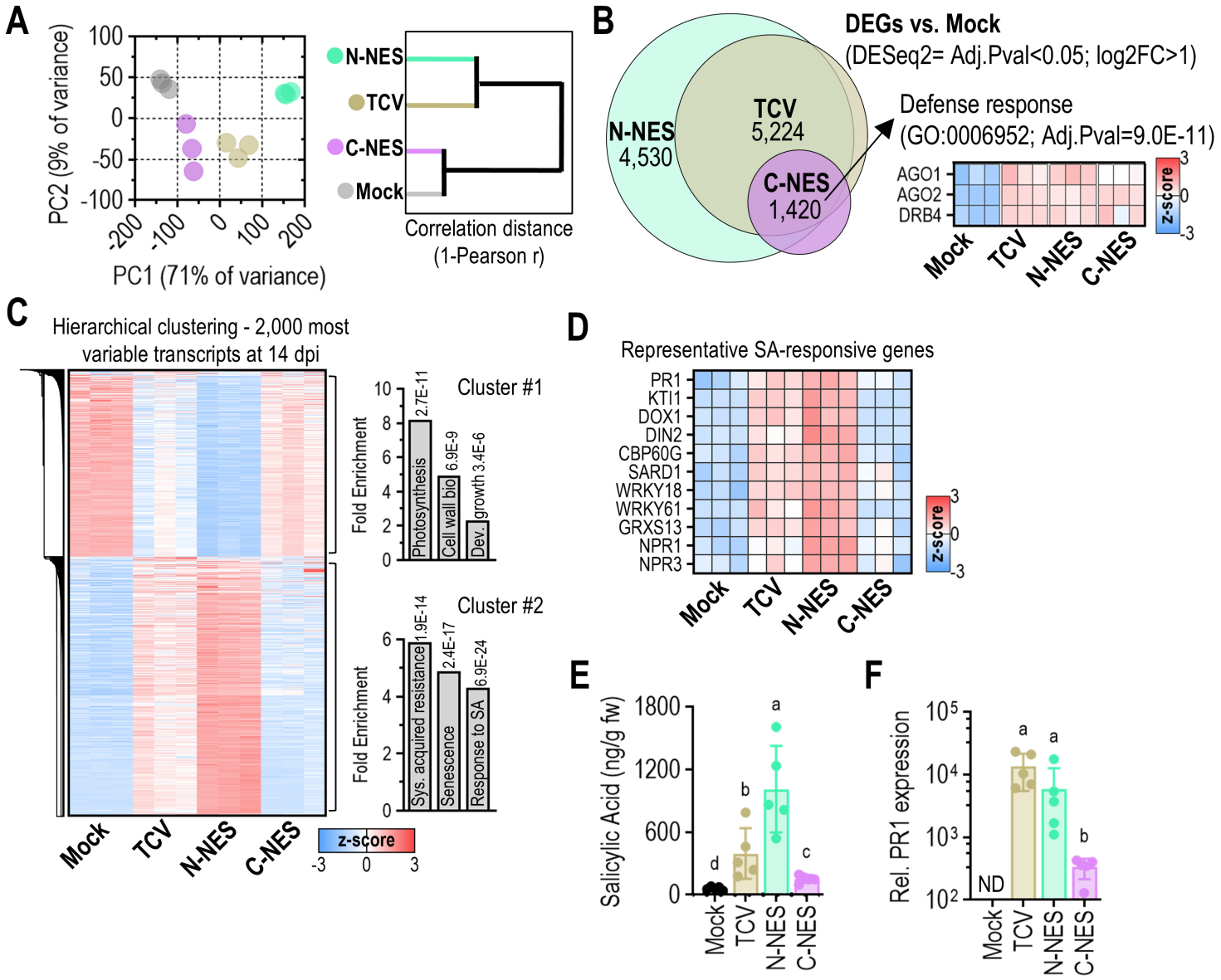


Figure 2

TCV CP variants differentially activate SA-associated host response.

(A) Principal component analysis (PCA) of expression profiles of mock or infected Col-0 plants at 14 dpi. Dendogram depicting treatment-level clustering using replicate averaged log2-CPM expression values. Pairwise distances were calculated as 1-Pearson's correlation coefficient, and hierarchical clustering was performed using average linkage. Branch lengths represent correlation distance. (B) Venn diagram of all DEGs identified in virus-infected plants vs Mock. Heat map of defense-associated genes previously implicated in TCV defense. (C) Heat-map of hierarchical clustering of the top 2,000 DEGs identified by DESeq2. Gene ontology analysis of biological processes of each cluster identified up-regulated and down-regulated pathways listed to the right. Bar graphs show fold-enrichment and adjusted p-values of selected pathways (D) Heat-map of expression of representative SA-responsive genes in infected Col-0 plants. (E) Free SA accumulation quantified by Acinetobacter sp. ADPWH-lux biosensor (n=5). (F) PR1

expression measured by RT-qPCR (n=5). Data in panels E and F represent the median values across at least two independent experiments. Lognormal one-way ANOVA with Tukey's multiple comparison test was used for statistical analyses.

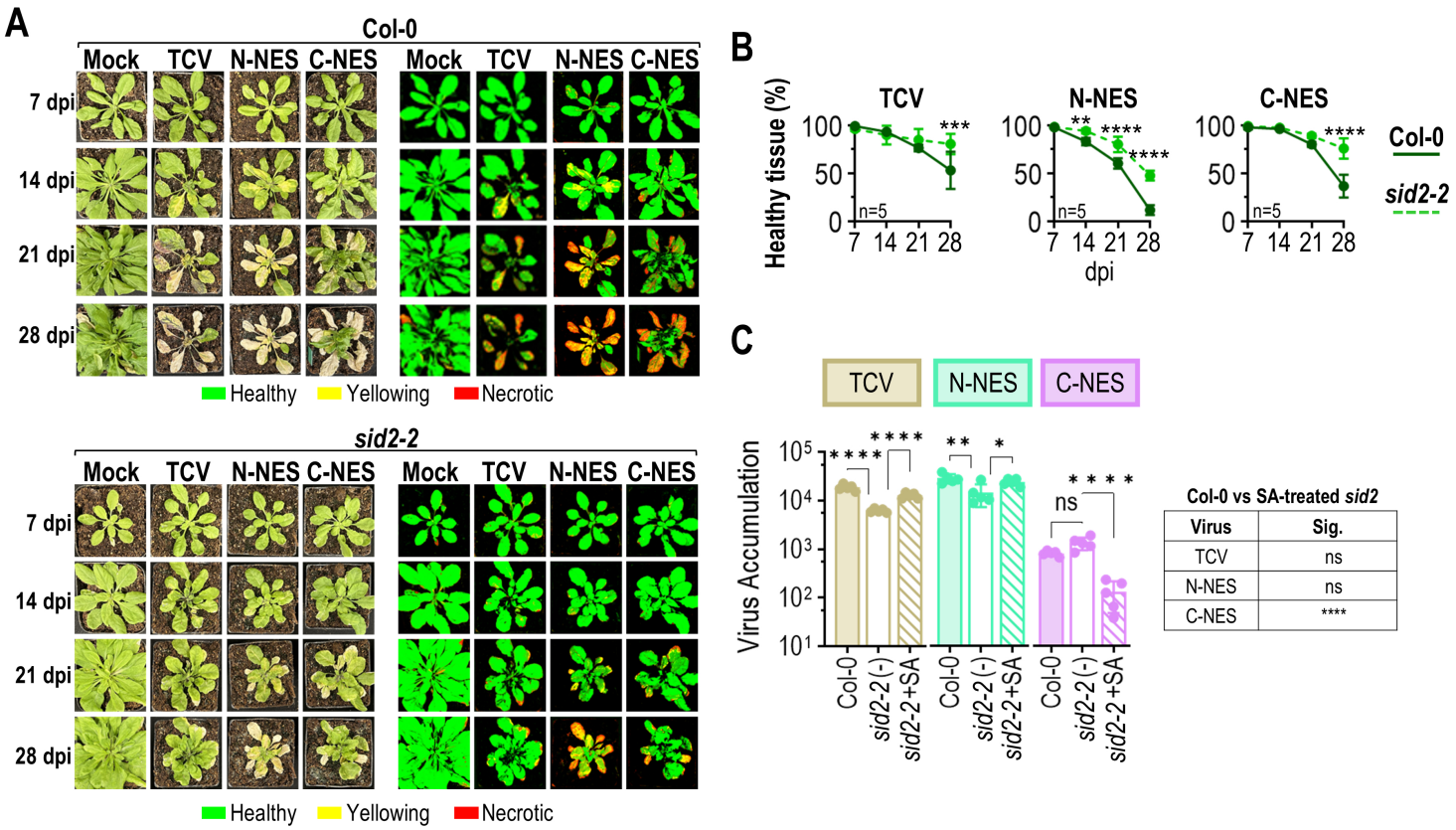


Figure 3

Salicylic acid drives TCV-associated disease but has CP-dependent effects on viral accumulation.

(A) Time-course of infected Col-0 and sid2-2 plants with corresponding disease image segmentation indicating healthy (green), chlorotic (yellow), and necrotic (red) tissue. (B) Percent healthy tissue of infected whole plants calculated via ImageJ segmentation analysis at indicated time points (n=5). Statistical analysis compares healthy tissue percent between Col-0 (solid dark green line) and sid2-2 (dashed light green line) plants within each time point tested. Images are representative of plants from at least three independent experiments. (C) Virus accumulation measured by RT-qPCR in indicated condition (n=5). Col-0 plants were untreated (solid-colored bars), while sid2-2 plants were either untreated (-; solid white bars) or treated with salicylic acid (+SA; striped bars) beginning 24 hours post-infection until harvest at 14 dpi. Data in panels B and C represent the median measurements from at least three independent experiments. Lognormal one-way ANOVA with Tukey's multiple comparison used for statistical analysis. *p<0.05 **p<0.01 ****p<0.0001

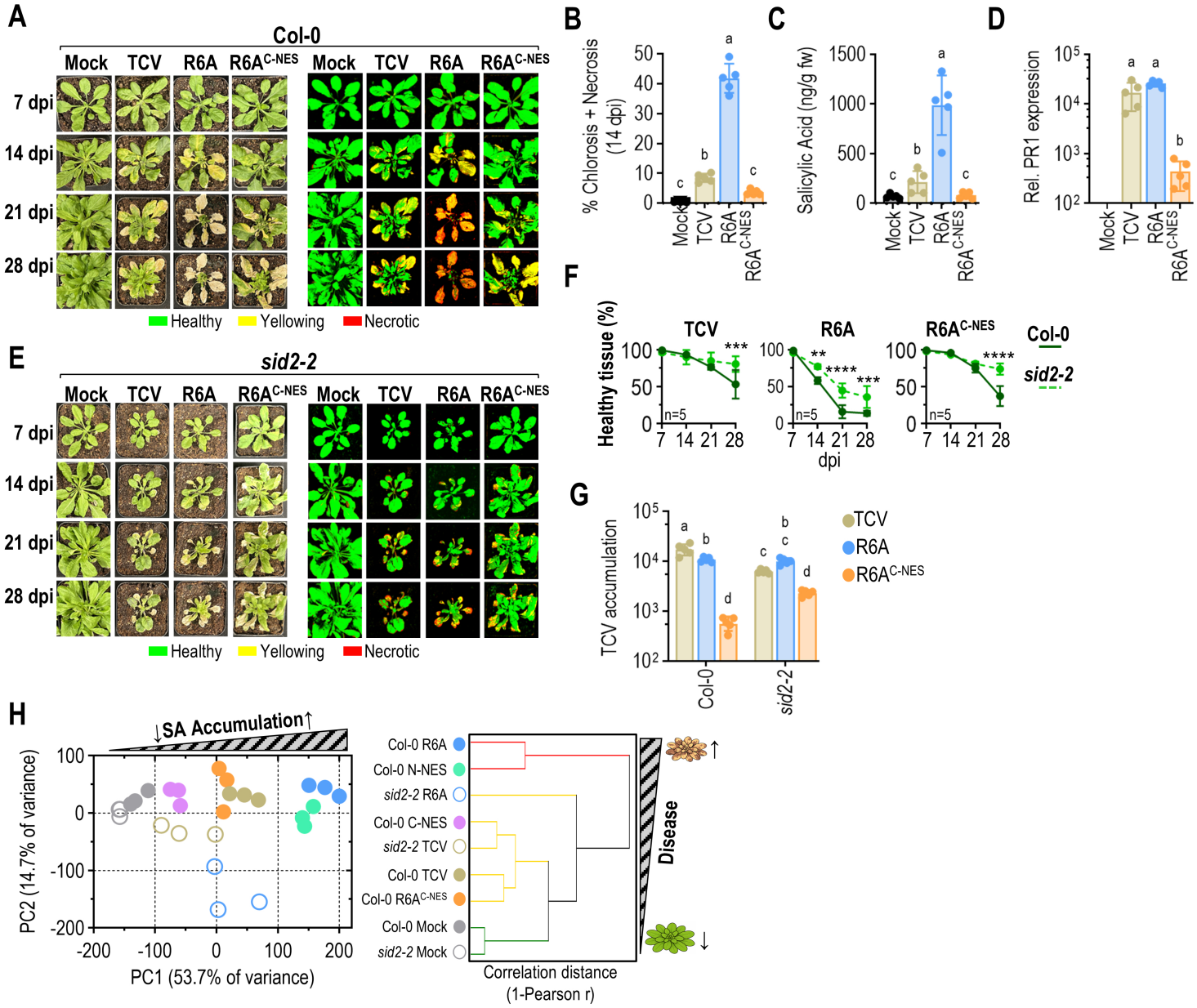


Figure 4

An N-terminal CP mutation uncouples SA-dependent disease from viral fitness.

(A) Time-course of representative Col-0 plants with corresponding disease image segmentation indicating healthy (green), chlorotic (yellow), and necrotic (red) tissue. (B) Percent chlorosis and necrosis of infected Col-0 plants at 14 dpi as calculated following ImageJ segmentation (n=5). (C) Free SA accumulation quantified by Acinetobacter sp. ADPWH-lux biosensor (n=5). (D) PR1 expression quantified by RT-qPCR of infected Col-0 at 14 dpi (n=5). (E) Time-course of representative sid2-2 plants with corresponding disease image segmentation. (F) Percent healthy tissue of infected Col-0 and sid2-2 plants calculated following ImageJ segmentation analysis at indicated time points. Statistical analysis compares healthy tissue percent between Col-0 (solid dark green line) and sid2-2 (dashed light green line) plants within each time point tested (n=5). (G) Virus accumulation measured by RT-qPCR at 14 dpi

(n=5). (H) PCA of gene expression profiles for TCV infections in Col-0 and sid2-2 plants. Dendrogram depicting treatment-level clustering using replicate averaged log2-CPM expression values. Red branches indicate severe disease, yellow branches indicate intermediate disease, while green branches indicate uninfected controls. Images in panels A and E are representative of plants from at least three independent experiments. Data in panels B, C, D, F, and G is representative of the median points across at least two independent experiments. Lognormal one-way ANOVA with Tukey's multiple comparison was used for all statistical analyses. **p<0.01 ***p<0.001 ****p<0.0001

Supplementary Files

This is a list of supplementary files associated with this preprint. Click to download.

- DataS1.xlsx
- DataS2.xlsx
- TableS1.docx